Morphology, structure, optical, and electrical properties of $AgSbO_3$

Z. G. Yi, Y. Liu, and R. L. Withers[a)]
Research School of Chemistry, The Australian National University, Canberra ACT 0200, Australia

(Received 6 April 2010; accepted 9 June 2010; published online 30 July 2010)

The morphology of defect pyrochlore-type, $AgSbO_3$ microparticle/nanoparticles obtained via solid state reaction evolve from irregular to Fullerene-like polyhedra before finally decomposing into metal-organic framework-5 like particles with increase in sintering temperature. The defect pyrochlore-type $AgSbO_3$ particles are slightly Ag deficient while the valence of the antimony ion is shown to be +5 giving rise to a probable stoichiometry of $Ag_{1-x}Sb^{V}O_{3-x/2}$, with $x \sim 0.01-0.04$. A highly structured diffuse intensity distribution observed via electron diffraction is interpreted in terms of correlated displacements of one-dimensional (1D) silver ion chains along ⟨110⟩ directions. A redshifting in the absorption edges in UV-visible absorption spectra is observed for samples prepared at sintering temperatures higher than 1000 °C and attributed to the surface plasma resonance effect associated with small amounts of excess metallic Ag on the $Ag_{1-x}Sb^{V}O_{3-x/2}$ particles. An electrical properties investigation of the silver antimonate samples via dielectric, conductivity, and electric modulus spectroscopy shows a prominent dielectric relaxation associated with grain boundaries. The silver ion conductivity is associated with correlated displacements of 1D silver ion chains along ⟨110⟩ directions. © *2010 American Institute of Physics*.
[doi:10.1063/1.3462434]

I. INTRODUCTION

Antimonates exhibit an intriguing range of excellent electrical, optical, and catalytic properties.[1–9] $AgSb^{V}O_3$, for instance, is known to be a Ag^+ fast ion conductor while autoreduction upon thermal treatment has been shown to lead to mixed ionic and electronic conductivity.[4] In amorphous thin film form, it is known to be a novel transparent electroconductive semiconductor[1–3] while $AgSbO_3$ ceramics loaded with additional CuO exhibit excellent thermoelectric properties.[5] Furthermore, $AgSb^{V}O_3$ has more recently been shown to absorb visible light up to 480 nm and to act as a novel visible-light sensitive photocatalyst.[7] In addition, $AgSb^{V}O_3$ is commonly used to form solid solutions for lead free ferroelectric and piezoelectric applications.[10–12] The potential for applications of such antimonates as well as their bonding properties have also stimulated research on their synthesis and structure.[13–19]

$AgSbO_3$ can be obtained either via solid state reaction of Ag_2O and Sb_2O_3 or by ion exchange of $AgNO_3$ and as prepared $NaSbO_3$.[7,16] Unlike M^+NbO_3 and M^+TaO_3 perovskites, M^+SbO_3 compounds usually do not form structures having 180° Sb–O–Sb linkages (e.g., perovskite type structures) owing to an especially strong $Sb^{5+}-O^{2-}$ covalent interaction.

Over recent years, tremendous efforts have been directed toward the development of synthetic procedures for producing inorganic (in particular, metallic) particles such as Ag, Au, Pt, Cu_2O, and ZnO with controlled shapes and sizes.[20–24] Nanostructures or particles with a wide range of morphologies have been fabricated using various synthetic approaches, e.g., changing the precursor ratio in the polyol process, the introduction of new inorganic starting species and seed-induced growth.[24–26] Despite much success in the synthesis of inorganic nanocrystals, the preparation, and shape control of microstructures or nanostructures of antimonates has not yet been reported. Moreover, understanding of the local crystal structure and the associated mechanism for silver ion conductivity in silver antimonate is still very limited.

In the present study, we first demonstrate the controlled synthesis of silver antimonate particles with a fullerene-like morphology by a simple solid state reaction process, and then investigate its local crystal chemistry via electron diffraction. In addition, its optical properties as well as its silver ion conductivity are also studied via UV-visible absorption measurements in conjunction with dielectric, conductivity, and electric modulus spectroscopy.

II. EXPERIMENTAL

A. Sample preparation

$AgSb^{V}O_3$ powders with various morphologies were obtained by solid state reaction of stoichiometrically mixed Ag_2O (99.99% purity) and $Sb_2^{III}O_3$ (99.99% purity) oxide powders at 800–1100 °C in air for 2 h. $AgSbO_3$ ceramics were obtained by crushing 800 °C-presintered powders, pressing into disks and then sintering at 900 °C in air for a further 2 h. During the fabrication of these samples, rapid heating (30 °C/min) and cooling (20 °C/min) techniques were employed.

B. Sample characterization

The morphology and structure of the prepared samples were then investigated using scanning electron microscopy (SEM) and x-ray powder diffraction (XRD), respectively. The elemental composition of the samples was analyzed both by energy-dispersive x-ray spectroscopy (EDX) (using pure Ag_2O and Sb_2O_5 as compositional standards) and x-ray pho-

a)Electronic mail: withers@rsc.anu.edu.au.

toelectron spectroscopy (XPS). The chemical valence state of the antimony was investigated via XPS. XRD patterns were recorded using a Siemens D-5000 diffractometer and Cu $K\alpha$ radiation.

XPS of the valence band and of the principal core levels of the silver antimonate were measured on an ESCALAB220i-XL x-ray photoelectron spectroscope, using monochromated Al $K\alpha$ as the excitation source. The photoelectron spectra as a function of binding energy were analyzed over the energy range 0–1100 eV by a concentric hemispherical analyzer at a constant analyzer energy of 20 eV for high-resolution region scans. Under these conditions, the spectrometer results in an energy resolution of about 0.6 eV for the Ag $3d_{5/2}$ line from clean silver samples. The carbon C $1s$ peak (285.0 eV) was applied for binding energy calibration. Concentration quantification was done with the standard single element sensitivity factors from the THERMO SCIENTIFIC AVANTAGE software. The standard atomic concentration calculation provides a ratio of each component to the sum of the others taking into account the elements in the data. Only those elements for which the specific line is clearly visible in the spectrum are considered. For those lines the background is subtracted using the Shirley method. The limit of the region of the line is individually selected and then the integration is done. The peak shapes were fitted after a background subtraction using a Gaussian function.

Samples for transmission electron microscopy (TEM) were ultrasonically dispersed in water-free ethanol and then transferred to carbon coated copper grids. Selected area electron diffraction experiments were carried out on a Philips EM430 TEM operating at 300 kV.

The diffuse reflectance UV-visible spectra were measured on a Varian Cary 5E UV-Vis-NIR spectrophotometer using the diffuse reflection method.

For electrical measurements, the surfaces of the ceramic pellets were first polished after which silver electrodes were applied. The alternating current and dc electrical properties were measured on a HP4184A impedance analyzer and a multimeter, respectively, in air at a heating rate of 3 °C/min.

III. RESULTS AND DISCUSSION

A. Particle composition and morphology

SEM images of the samples given in Fig. 1 show the intriguing morphological evolution of the $AgSbO_3$ particles prepared by sintering at various temperatures for 2 h. For the samples prepared at 800 °C [Fig. 1(a)], the particle size is relatively small (~500 nm) with blurry crystal edges. With increasing temperature, the particles grew larger and the crystal faces became clearer [as shown in Fig. 1(b)]. When the sintering temperature was increased to 1000 °C, Fullerene-like polyhedra with a particle size of ~1 um exhibiting clear faceting and sharp edges were observed everywhere [see Figs. 1(c) and 1(d)]. Most of the Fullerene-like polyhedra still remained at 1100 °C [Figs. 1(e) and 1(f)]. When the sintering temperature increased to 1200 °C, however, the polyhedra completely decompose and a metal-organic framework-5 (MOF-5) (Ref. 27) like morphology appears [as shown in Fig. 1(g)]. Compositional analysis via

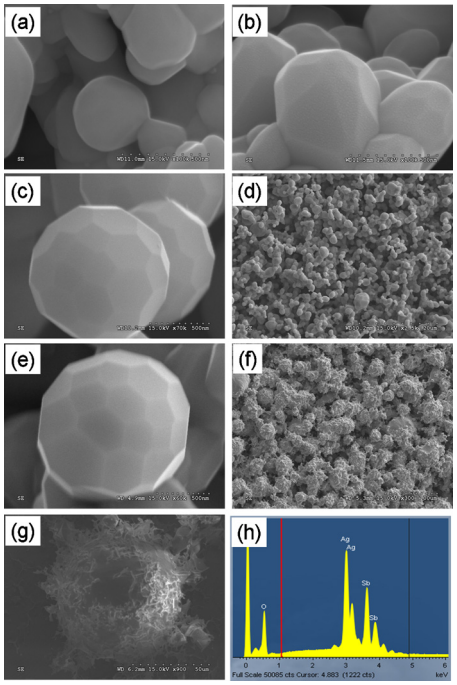

FIG. 1. (Color online) SEM images showing the morphological evolution of the silver antimonate particles obtained by sintering at various temperatures for 2 h: (a) 800 °C, (b) 900 °C, (c) 1000 °C, (d) 1000 °C on a larger scale, (e) 1100 °C, (f) 1100 °C on a larger scale, (g) 1200 °C, (h) a typical EDX spectrum of the Fullerene-like polyhedra obtained by sintering at 1050 °C. The two additional lines (red and black online) are used for identifying elements.

EDX of these MOF-5 like particles in conjunction with XRD analysis suggests that they are composed of inner balls of Ag surrounded by an outer Sb_2O_5 integument. Quantitative EDX analysis of the lower temperature Fullerene-like polyhedra using pure Ag_2O and Sb_2O_5 as compositional standards showed that they are composed of Ag, Sb, and O with atomic ratios of $(1-x):1.00:3.00$ (with x varying from 0.01 to 0.04).

B. XRD patterns and average structure

As is apparent from the XRD traces shown in Fig. 2, only $Ag_{1-x}SbO_{3-x/2}$ with a pyrochlore-type cubic structure (space group:Fd-3m, lattice parameter $a \sim 1.027$ nm) was

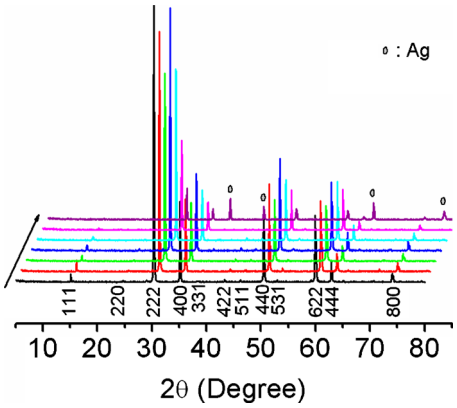

FIG. 2. (Color online) XRD patterns of samples prepared by sintering at temperatures ranging from 800 to 1100 °C, at intervals of 50 °C along the arrow direction.

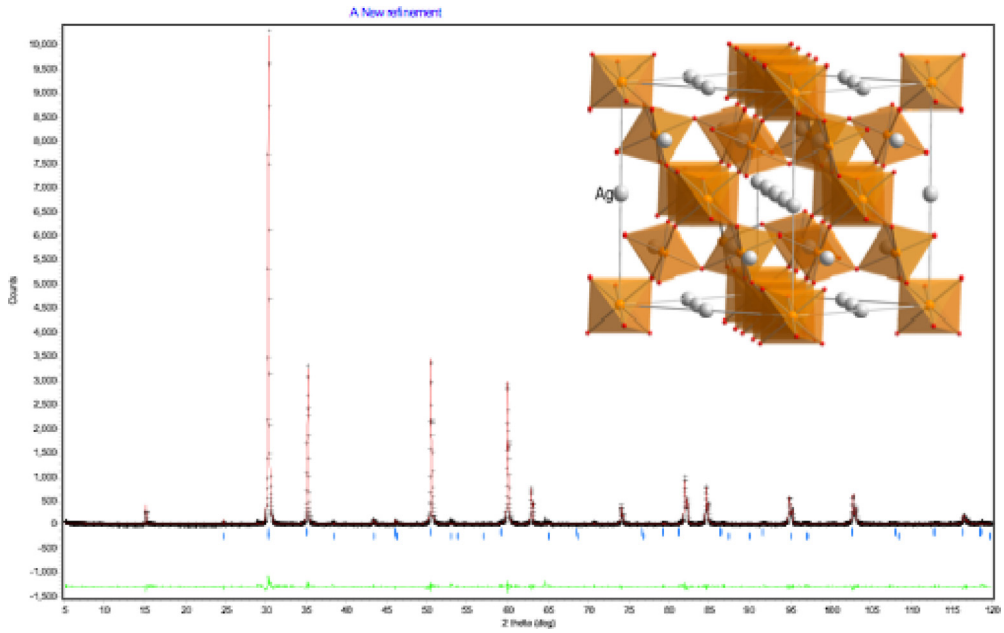

FIG. 3. (Color online) Rietveld refinement of the structure of the 900 °C sintered $AgSbO_3$ powder sample ($Rp=9.8\%, Rwp=16.4\%, x^2=1.7$). The observed and calculated patterns are indicated by crosses and the solid line, respectively. The difference curve is shown at the bottom on the same scale. The tick marks indicate the calculated positions of reflections. The inset shows the structure (Ref. 16) of $Ag_2Sb_2O_6\square$.

detected for samples prepared in the temperature range 800–1050 °C. (Attempts were made to synthesize the $Ag_{1-x}SbO_{3-x/2}$ phase in air at a temperature lower than 800 °C but were unsuccessful). For the sample prepared at 1100 °C, however, a second phase corresponding to excess Ag metal was clearly observed. Sintering the sample at an even higher temperature (1200 °C) resulted in the complete disappearance of the $Ag_{1-x}SbO_{3-x/2}$ phase.

The average crystal structure of $AgSbO_3$, usually written in the form $Ag_2Sb_2O_6\square_1$ (where $\square$ represents a vacancy) to emphasize its relationship to the *Fd*-3*m*, ideal cubic pyrochlore structure type, was recently reported by Mizoguchi *et al.*[16] It can be described in terms of an essentially rigid Sb_2O_6 framework substructure defined by a vertex-sharing network of SbO_6 octahedra running through which are interpenetrating parallel tunnels running along the crystallographic ⟨110⟩ directions, as shown in Fig. 3. These interpenetrating channels are occupied by Ag ions (located on the Wyckoff 16*d* sites). The oxygen ions in the vertex-sharing octahedral framework sit on the Wyckoff 48*f* sites. They are coordinated to two Sb and two Ag cations in a highly distorted tetrahedral type environment. Rietveld refinement of our sample is consistent with this average structure model (Fig. 3).

C. XPS spectra

The composition of the as prepared samples, in particular the valence state of the antimony ion, was also checked by XPS analysis. Figure 4(a) shows a survey scan XPS spectra of one sample. The peaks arising from silver antimonate (Sb 4*d*, 4*s*, 3*d*, 3*p*, Ag 3*d*, 3*p*, O 1*s*, etc.) are readily apparent. A small contaminant C 1*s* peak is also evident. This was used for energy calibration. The surface stoichiometry was quantified from the spectrum. The measured atomic concentrations of Ag, Sb, and O were consistent with the results obtained above from EDX, indicating a slight loss of silver.

The nominal possibility of a mixed (+3,+5) valence state for the antimony ions was also investigated via XPS (see the high-resolution XPS spectra taken for the spin-orbit doublet of Sb 3*d* shown in Fig. 4(b)]. The two strong peaks

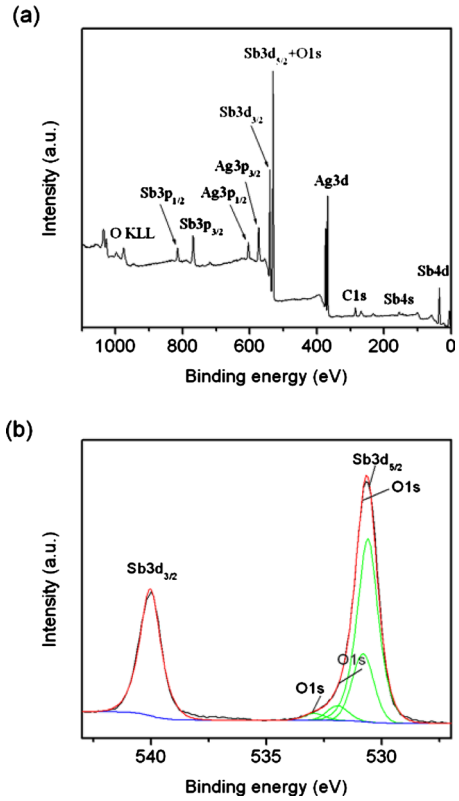

FIG. 4. (Color online) (a) A typical low resolution survey scan XPS spectra of the 900 °C sintered sample. (b) The corresponding high-resolution XPS spectra taken to highlight the spin-orbit doublet region of Sb 3*d*.

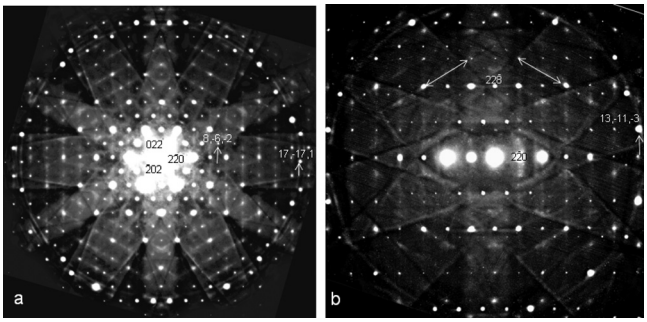

FIG. 5. Typical EDPs of the 900 °C sintered $AgSbO_3$ sample taken along the (a) ⟨111⟩ and (b) ⟨221⟩ zone axis directions. Note the highly structured diffuse streaking apparent in both EDPs.

located at 540.1 eV and 530.6 eV are assigned to Sb $3d_{3/2}$ and Sb $3d_{5/2}$, respectively. The binding energy of 530.6 eV is consistent with that of antimony with a +5 valence state.[28] In order to analyze the composition in detail, curve fitting to the spectra was performed. The experimental curve at about 540 eV could be well fitted with a single Gaussian peak whereas fitting to the curve at about 530 eV required one principal peak (at 530.1 eV) as well as three subpeaks on the higher energy side. The additional subpeaks were assigned to O 1*s* levels. No peaks corresponding to the +3 valence state of antimony (529.2 eV) could be detected in any of the samples. The stoichiometry of the silver antimonate is thus taken to be $Ag_{1-x}Sb^{V}O_{3-x/2}$, $x \sim 0.01-0.04$.

D. Electron diffraction

In order to obtain some insight into the mechanism of Ag^+ ion conductivity in $Ag_{1-x}Sb^{V}O_{3-x/2}$, electron diffraction was used to search for evidence of correlated Ag^+ ion displacements in the form of a structured diffuse intensity distribution. In addition to the strong Bragg reflections of the *Fd*-3*m* average structure, the $Ag_{1-x}Sb^{V}O_{3-x/2}$ samples are characterized by the presence of a highly structured diffuse intensity distribution in the form of $\mathbf{G} \pm \{110\}^*$ sheets of diffuse intensity (**G** an average structure Bragg reflection) running perpendicular to each of the six ⟨110⟩ directions of reciprocal space, see Fig. 5. (A very similar structured diffuse intensity distribution has been observed in other displacively disordered pyrochlores such as, e.g., $Bi_2In_2O_7$ (Ref. 29) and $Bi_2Sc_2O_7$ (Ref. 29) but not to date in "defect pyrochlores" of the current $Ag_{1-x}Sb^{V}O_{3-x/2}$ type.)

Figure 5, for example, shows typical (a) ⟨111⟩ and (b) ⟨221⟩ zone axis electron diffraction patterns (EDPs) of $Ag_{1-x}Sb^{V}O_{3-x/2}$ ($x \sim 0.01$). Characteristic, transverse polarized,[15] sharp diffuse streaking running through selected parent Bragg reflections, **G**, perpendicular to one or other of the six ⟨110⟩ directions of real space is apparent in both (a) and (b). In Fig. 5(a), for example, diffuse streaking occurs running through particular parent Bragg reflections, G, along the $\varepsilon[2,2,\bar{4}]^*$, $\varepsilon[\bar{4},2,2]^*$ and $\varepsilon[2,\bar{4},2]^*$, ε continuous, directions of reciprocal space, perpendicular to the $[1,\bar{1},0]$, $[0,1,\bar{1}]$, and $[\bar{1},0,1]$ real space directions, respectively. The continued presence of diffuse streaking of this type despite the changing incident beam orientation from (a) and (b) demonstrates that the streaking is not localized to that particular reciprocal space direction but rather forms part of $\{110\}^*$ sheets of diffuse intensity in reciprocal space perpendicular to each of the ⟨110⟩ directions of real space.

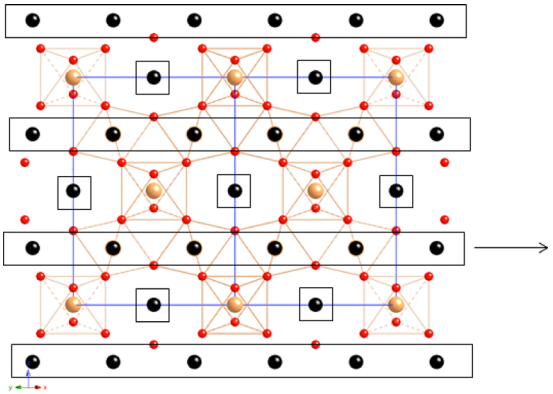

FIG. 6. (Color online) The *Fd*-3*m* average structure of $AgSb^{V}O_3$ shown in projection down a $\langle 1,-1,0\rangle$ direction. The essentially rigid (Sb_2O_6) octahedral corner-connected substructure array is shown in outline while the Ag^+ ions are shown as large balls. The observed $\mathbf{G} \pm \{110\}^*$ diffuse distribution (see Fig. 5) implies that all the silver ions within the rectangular 1D ⟨110⟩ boxes shown here move together in a linear chain along the relevant ⟨110⟩ direction by exactly the same amount while there is no correlation at all between the displacements of neighboring such boxes.

The fact that the intensity of the observed diffuse streaking is always strongest when looking out along directions of reciprocal space perpendicular to the direction of the streaking itself but goes to zero when looking along the direction of the streaking itself [most apparent in Fig. 5(a)], shows not only that the major contribution to the observed diffuse distribution necessarily arises from displacive disorder but also that the displacement of the atom/s involved is necessarily along the ⟨110⟩ real space directions perpendicular to each of the six $\{110\}^*$ sheets of diffuse intensity. Sharp $\{110\}^*$ sheets of diffuse intensity in reciprocal space imply ⟨110⟩ columns of atoms in real space whose displacive shifts are correlated along the corresponding ⟨110⟩ column direction but exhibit no transverse correlation from one such ⟨110⟩ column to the next.

Note furthermore that there are clear "extinction conditions" associated with this diffuse streaking, e.g., the diffuse streaking along the $\mathbf{G} \pm \varepsilon[2,2,\bar{4}]^*$ direction in Fig. 5(a) only runs through parent $\mathbf{G}=[hkl]^*$ reflections for which $h-k=4$ J, J an integer such as, e.g., $[8,\bar{8},0]^*$ but not through reflections such as $[8,\bar{6},\bar{2}]^*$, etc. Characteristic pseudoextinction conditions of this type arise because of the correlated displacement along ⟨110⟩ of heavily scattering Ag ions separated by integer multiples of 1/4 ⟨110⟩ along the column direction (see Fig. 6). Consider, for example, the *Fd*-3*m* average structure of $Ag_{1-x}Sb^{V}O_{3-x/2}$ shown in projection down a $\langle 1,\bar{1},0\rangle$ direction in Fig. 6. The essentially rigid (Sb_2O_6) octahedral corner-connected substructure array is shown in outline while the black Ag^+ ions are shown as black balls. The observed diffuse distribution implies that all the silver ions within the rectangular one-dimensional (1D) ⟨110⟩ boxes shown in Fig. 6 move together in a linear chain along the relevant ⟨110⟩ direction by exactly the same amount

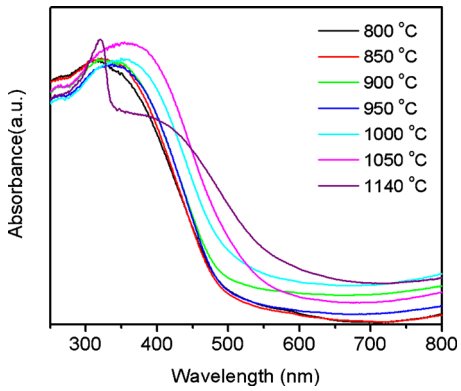

FIG. 7. (Color online) The UV-vis spectra of samples prepared at various temperatures.

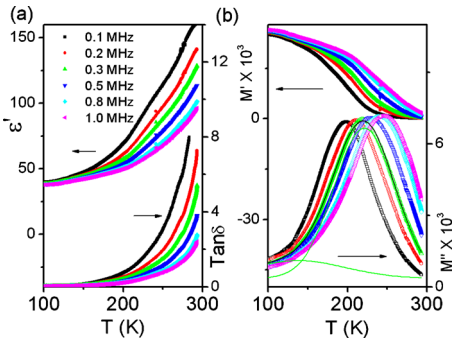

FIG. 8. (Color online) Temperature dependence of the electrical properties of the silver antimonate ceramic sample: (a) dielectric spectroscopy and (b) electric modulus spectroscopy. P_L and P_H subpeaks were fitted using Gaussian functions.

while there is no correlation at all between the displacements of neighboring such boxes. Note that when viewed along the orthogonal [110] direction the rectangular boxes outlined in Fig. 6 become the small square box also shown in Fig. 6. The existence of such correlated displacive chain motion is likely to be closely associated with the Ag^+ fast ion conduction properties of this material.

E. UV-visible absorption

The UV-vis spectra of the various samples as a function of sintering temperature are shown in Fig. 7. In general, the UV-vis absorption edge reflects the gap between the valence band and the conduction band of a semiconductor, with the band gap determined by the configuration of the constituent elements or the coordination symmetry of the metal atoms.[30,31] When a semiconductor forms a composite structure with small quantities of adsorbed noble metal particles such as Ag, the measured UV-vis absorption spectrum can be changed owing to the surface plasma resonance effect associated with the adsorbed Ag particles.[32,33] The measured UV-vis spectra should thus also be sensitive to the small differences between the various as prepared silver antimonates.

As anticipated, the UV-vis spectra in Fig. 7 can be divided into two different categories. For the samples prepared below 950 °C, where Ag depletion is minimal, the absorption edges are very similar. The measured absorption edge in this case can be attributed to the intrinsic absorption between the top of the valence band and the bottom of the conduction band of essentially stoichiometric $AgSbO_3$. For the samples prepared at sintering temperatures higher than 1000 °C, however, the surface plasmon resonance effect of the excess metallic Ag particles leads to a noticeable redshifting in the observed absorption edges. For the sample heat treated at 1140 °C, two absorption edges appear since the nominal $Ag_{1-x}Sb^{V}O_{3-x/2}$ sample has completely decomposed into a mixture of Ag metal and Sb_2O_5 and the latter is a wide band gap semiconductor with a white color.

F. Electrical properties

Dielectric, conductivity, and electric modulus spectroscopy were also performed on the $Ag_{1-x}Sb^{V}O_{3-x/2}$ ($x \sim 0.0$ to 0.04) ceramic samples to investigate the dielectric relaxation as well as the transportation mechanism of this Ag^+ ion conductor.

Figure 8(a) shows the measured temperature dependence of the dielectric permittivity as well as the dielectric loss tangent (tan δ) at various frequencies. The rapid increase in both the dielectric permittivity as well as the dielectric loss tangent (tan δ) with temperature implies thermally activated leakage conductivity while the observed frequency dependence implies that the behavior of this leakage conductivity involves some sort of relaxation process involving mobile ions. To further clarify this relaxation behavior, electric modulus spectroscopy was also employed, as shown in Fig. 8(b). Note that frequency-dependent relaxation peaks are thereby observed.

Physically, the electric modulus corresponds to the relaxation of the electric field in the material when the electric displacement remains constant, so that the electric modulus represents the real dielectric relaxation process, which can be expressed as:[34]

$$M^*(\omega) = 1/\varepsilon^*(\omega) = M' + iM'' = M\infty\left[1 - \int_0^\infty \left(-\frac{d\phi(0)}{dt}\right)\exp(-i\omega t)dt\right], \quad (1)$$

where $M_\infty = (\varepsilon_\infty)^{-1}$ is the asymptotic value of $M'(\omega)$ and $\Phi(t)$ is the time evolution of the electric field within the material.

For a thermally activated relaxation process, the relaxation time generally follows the Arrhenius law:

$$\tau = \tau_0 \exp(E/k_B T), \quad (2)$$

where τ_0 is the pre-exponential factor (or the relaxation time at infinite temperature), E denotes the activation energy of the relaxation process, T is the absolute temperature, and k_B is the Boltzmann constant. It is well known that the condition $\omega_p \tau_p = 1$ is fulfilled at the peak position, where $\omega = 2\pi f$ is the angular frequency of measurement and the subscript p denotes the values at the peak position. By plotting $\ln(\omega_p)$ as a function of the reciprocal of the peak temperature, a linear relation should then be obtained according to Eq. (2). The relaxation parameters E and τ_0 can then be deduced from the slope and intercept of this line, respectively. Before this can be done, however, it is necessary to note that the M'' curves

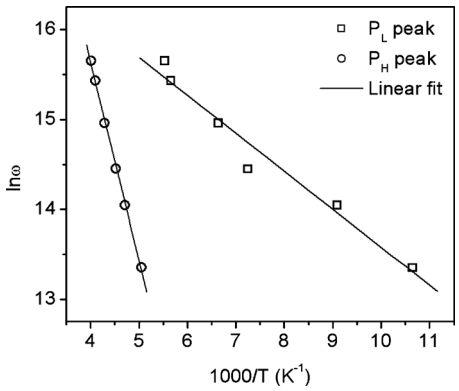

FIG. 9. Arrhenius plots for the electric modulus relaxation peaks, where the solid lines are the linear least-square fitting.

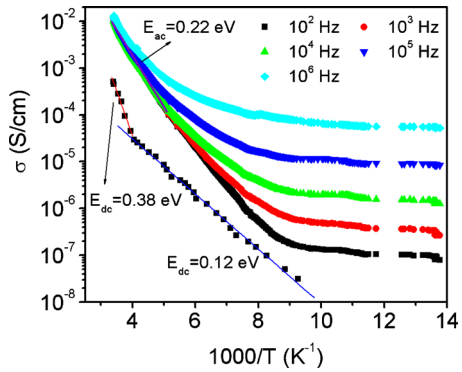

FIG. 11. (Color online) The temperature dependence of the ac and dc conductivities of the $AgSbO_3$ ceramic sample.

in Fig. 8(b) are asymmetric while there are two distinct regions of rapid decrease in the M' curves. The two distinct intervals in the M' curves suggest the presence of two subpeaks in the M'' curves. The frequency and temperature-dependent P_L and P_H subpeak positions (L for lower and H for higher) were then extracted using Gaussian fitting to the M'' curves.

Figure 9 shows ln ω versus $1000/T$ Arrhenius plots for these electric modulus relaxation peaks. The solid lines are linear least-square fittings. The relevant relaxation parameters for the P_L and P_H peaks are $E=0.04$ eV, $\tau_0=1.86\times10^{-8}$ s and $E=0.19$ eV, $\tau_0=2.36\times10^{-11}$ s, respectively.

For ionic conductors, plotting ac data such as impedance and electric modulus in the complex plane is extremely advantageous for distinguishing between these types of materials and in making the proper physical process assignments.[35–37] The complex impedance Z^* can be calculated from ε^* as follows: $Z^*=Z'-iZ''=1/i\omega C_0\varepsilon^*$, where ω is the angular frequency $\omega=2\pi f$ and $i^2=-1$. $C_0=\varepsilon_0 S/d$ is the vacuum capacitance, S is the sample area, and d the sample thickness. Figure 10 shows the complex impedance as well as the modulus spectra of the $AgSbO_3$ ceramic sample measured at 293 K and 75 K in air, respectively. From the limited

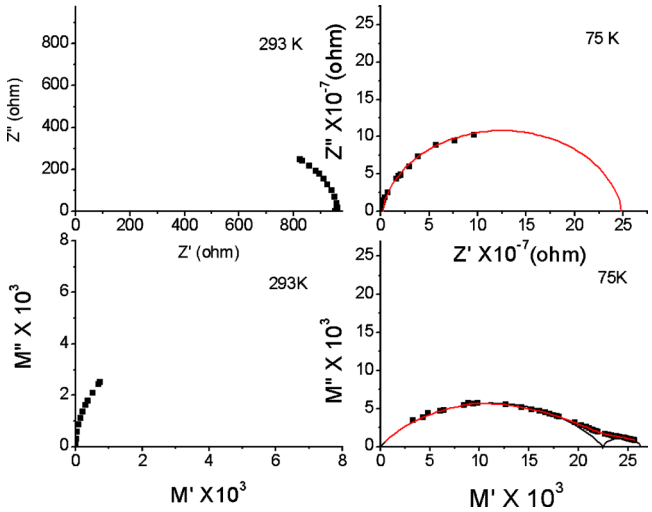

FIG. 10. (Color online) The complex impedance and electric modulus spectra of the 900 °C sintered $AgSbO_3$ specimen measured at 293 K and 75 K in air, respectively. The curves are used for guidance.

impedance data obtained over the investigated temperature and frequency intervals, it is difficult to distinguish between bulk and grain boundary effects. However, from the electric modulus data, especially that obtained at the lower temperature of 75 K, it appears that relaxation involving ionic motion in the grain boundary regions is dominant over the investigated temperature interval. This also makes it clear that the aforementioned P_L and P_H peaks correspond to grain interior (intrinsic) and grain boundary effects, respectively. The near zero activation energy for the grain interior (intrinsic) relaxation suggests that the Ag^+ ions on the 16*d* sites can very easily move along the ⟨110⟩ directions (see Fig. 6), presumably initially toward empty neighboring 8*b* sites but perhaps even passing from one 16*d* site to the next.

Finally, Fig. 11 shows the measured temperature dependence of the conductivity (both ac and dc). The observed variation in σ_{ac} with temperature can be divided into following two distinct regions: a frequency dispersive, low temperature region and a temperature dependent, high temperature region. In the lower temperature range, σ_{ac} shows strong frequency dispersion and weak temperature dependence. In this region, σ_{ac} increases with frequency. In the higher temperature range, σ_{ac} shows strong temperature dependence and weak frequency dependence. The activation energy E_{ac} calculated from the linear-part in σ_{ac} varied from 0.21 eV at 100 Hz to 0.23 eV at 1 MHz, consistent with the activation energy of grain boundary relaxation obtained from the electric modulus spectra.

The temperature dependence of the dc conductivity could also be divided into two intervals: low temperature impurity conductivity ($E_{dc}=0.12$ eV) and high temperature intrinsic conductivity ($E_{dc}=0.38$ eV). The reason that the activation energy for intrinsic conductivity is larger than that of the local relaxation is that intrinsic conductivity requires long-range ion migration. The measured values of σ_{dc} $\sim10^{-3}$ S/cm and σ_{ac} of $\sim10^{-2}$ S/cm close to room temperature suggest the material has promise for energy-orientated applications.

IV. CONCLUSIONS

In summary, silver antimonate particles with various morphologies, in particular a fullerene-like morphology, have been obtained via simple solid state reaction over the

temperature range 800–1100 °C. The silver antimonate particles obtained have a pyrochlore-type average structure with a cubic lattice parameter of ~1.027 nm. Both EDX and XPS data indicate a slight deficiency of Ag and a resultant stoichiometry of $Ag_{1-x}Sb^{V}O_{3-x/2}$ ($x \sim 0$ to 0.04) depending on the highest annealing temperature. High-resolution XPS spectra show that the antimony has the +5 valence state with no evidence for any peaks corresponding to the +3 valence state detected. A highly structured diffuse intensity distribution observed in addition to the strong Bragg reflections of the underlying average structure requires correlated displacements of Ag^{+} ions along the ⟨110⟩ real space directions. UV-vis spectra show a noticeable redshifting in the measured absorption edges for the samples annealed at temperatures higher than 1000 °C. This is attributed to increasing Ag ion deficiency at higher temperatures leading to the deposition of small Ag particles onto the surface of the much larger $Ag_{1-x}Sb^{V}O_{3-x/2}$ particles. In turn, the surface plasma resonance effect of these deposited Ag metal particles leads to the observed redshifting in the measured absorption edges. Finally, the electrical properties of the silver antimonates have been studied with dielectric, conductivity, and electric modulus spectroscopy. It is found that grain boundary dielectric relaxations are prominent and that the silver ions on the 16*d* Wyckoff sites can move nearly freely along the ⟨110⟩ directions of the average structure.

ACKNOWLEDGMENTS

Z.G.Y., Y.L., and R.L.W. acknowledge financial support from the Australian Research Council (ARC) in the form of ARC Discovery Grants.

[1]M. Yasukawa, H. Hosono, N. Ueda, and H. Kawazoe, Jpn. J. Appl. Phys., Part 2 **34**, L281 (1995).
[2]M. Yasukawa, H. Hosono, N. Ueda, and H. Kawazoe, J. Ceram. Soc. Jpn. **103**, 455 (1995).
[3]H. Hosono, M. Yasukawa, and H. Kawazoe, J. Non-Cryst. Solids **203**, 334 (1996).
[4]H. Wiggers, U. Simon, and G. Schon, Solid State Ionics **107**, 111 (1998).
[5]S. Nishiyama, A. Ichikawa, and T. Hattori, J. Ceram. Soc. Jpn. **112**, 298 (2004).
[6]H. Mizoguchi and P. M. Woodward, Chem. Mater. **16**, 5233 (2004).
[7]T. Kako, N. Kikugawa, and J. H. Ye, Catal. Today **131**, 197 (2008).
[8]J. Singh and S. Uma, J. Phys. Chem. C **113**, 12483 (2009).
[9]J. Sato, N. Saito, H. Nishiyama, and Y. Inoue, J. Photochem. Photobiol. Chem. **148**, 85 (2002).
[10]Y. Saito, H. Takao, T. Tani, T. Nonoyama, K. Takatori, T. Homma, T. Nagaya, and M. Nakamura, Nature (London) **432**, 84 (2004).
[11]D. M. Lin, K. W. Kwok, and H. L. W. Chan, J. Appl. Phys. **106**, 034102 (2009).
[12]Y. Y. Wang, Q. B. Liu, J. G. Wu, D. Q. Xiao, and J. G. Zhu, J. Am. Ceram. Soc. **92**, 755 (2009).
[13]A. W. Sleight, Mater. Res. Bull. **4**, 377 (1969).
[14]H. Y.-P. Hong, J. A. Kafalas, and J. B. Goodenough, J. Solid State Chem. **9**, 345 (1974).
[15]R. L. Withers, Adv. Imaging Electron Phys. **152**, 303 (2008).
[16]H. Mizoguchi, P. M. Woodward, S. H. Byeon, and J. B. Parise, J. Am. Chem. Soc. **126**, 3175 (2004).
[17]V. B. Nalbandyan, M. Avdeev, and A. A. Pospelov, Solid State Sci. **8**, 1430 (2006).
[18]G. Blasse, J. Inorg. Nucl. Chem. **26**, 1191 (1964).
[19]J. B. Goodenough and J. A. Kafalas, J. Solid State Chem. **6**, 493 (1973).
[20]A. Tao, P. Sinsermsuksakul, and P. D. Yang, Angew. Chem., Int. Ed. **45**, 4597 (2006).
[21]F. Kim, S. Connor, H. Song, T. Kuykendall, and P. D. Yang, Angew. Chem., Int. Ed. **43**, 3673 (2004).
[22]T. Herricks, J. Y. Chen, and Y. N. Xia, Nano Lett. **4**, 2367 (2004).
[23]M. J. Siegfried and K. S. Choi, Adv. Mater. **16**, 1743 (2004).
[24]F. R. Fan, Y. Ding, D. Y. Liu, Z. Q. Tian, and Z. L. Wang, J. Am. Chem. Soc. **131**, 12036 (2009).
[25]T. Mokari, M. J. Zhang, and P. D. Yang, J. Am. Chem. Soc. **129**, 9864 (2007).
[26]S. H. Im, Y. T. Lee, B. Wiley, and Y. N. Xia, Angew. Chem., Int. Ed. **44**, 2154 (2005).
[27]N. L. Rosi, J. Eckert, M. Eddaoudi, D. T. Vodak, J. Kim, M. O'Keeffe, and O. M. Yaghi, Science **300**, 1127 (2003).
[28]J. Chastain, *Handbook of X-Ray Photoelectron Spectra* (PerkinElmer, Eden Prairie, MN, 1992).
[29]Y. Liu, R. L. Withers, H. B. Nguyen, K. Elliott, Q. Ren, and Z. Chen, J. Solid State Chem. **182**, 2748 (2009).
[30]M. A. Butler, J. Appl. Phys. **48**, 1914 (1977).
[31]G. Blasse, *Structure and Bonding* (Springer Verlag, Berlin), Vol. **42**, 1 (1980).
[32]N. Ji, W. D. Ruan, C. X. Wang, Z. C. Lu, and B. Zhao, Langmuir **25**, 11869 (2009).
[33]A. C. Patel, S. X. Li, C. Wang, W. J. Zhang, and Y. Wei, Chem. Mater. **19**, 1231 (2007).
[34]P. B. Macedo, C. T. Moynihan, and R. Bose, Phys. Chem. Glasses **13**, 171 (1972).
[35]R. Gerhardt, J. Phys. Chem. Solids **55**, 1491 (1994).
[36]Z. G. Yi, Y. X. Li, Y. Wang, and Q. R. Yin, J. Electrochem. Soc. **153**, F100 (2006).
[37]Z. G. Yi, Y. X. Li, Y. Wang, and Q. R. Yin, Appl. Phys. Lett. **88**, 162908 (2006).